RSC Advances

ROYAL SOCIETY OF CHEMISTRY

www.rsc.org/advances

RSC Advances

ARTICLE

Tube-like α-Fe_2O_3@Ag/AgCl Heterostructure: Controllable Synthesis and Enhanced Plasmonic Photocatalytic Activity†

Received 00th January 20xx,
Accepted 00th January 20xx

DOI: 10.1039/x0xx00000x

www.rsc.org/

Jun Liu,[a, b] Wei Wu,[a, b, c*] Qingyong Tian,[a, b] Shuanglei Yang,[b] Lingling Sun,[a, b] Xiangheng Xiao,[a*] Feng Ren,[a] Changzhong Jiang[a] and Vellaisamy A.L. Roy[c*]

Abstract: Plasmonic photocatalysts coupled with semiconductors are one of the most popular combinations in environmental remediation applications. In this regard, a novel tube-like α-Fe_2O_3@Ag/AgCl hybrid structures are fabricated via anchoring Ag/AgCl hybrid nanoparticles on the surface of α-Fe_2O_3 short nanotubes (SNTs) by a step-by-step strategy. Firstly, the monodispersed α-Fe_2O_3 SNTs have been synthesized via an anion-assisted hydrothermal process followed by the loading of Ag nanoparticles on the surface of α-Fe_2O_3 SNTs through the classic silver mirror reaction mechanism. From *in situ* oxidation of Ag nanoparticles, the final product α-Fe_2O_3@Ag/AgCl heterostructures have been obtained. We study the morphology, composition, and photocatalytic properties of as obtained tube-like α-Fe_2O_3@Ag/AgCl nano-heterostructures. The photocatalytic activities of as obtained photocatalysts have been tested by the degradation of organic dye Rhodamine B (RhB) under the simulated sunlight (UV + visible light), visible light and UV light irradiation. The main reason for the enhanced photocatalytic performance is attributed to the broad spectral response from the combination of narrow/wide bandgap semiconductors with metallic Ag nanoparticles and efficient charge transfer from plasmon-excited Ag nanoparticles to α-Fe_2O_3 and AgCl. Finally, this hybrid structure provides a roadmap for the controlled synthesis of plasmonic photocatalysts with excellent properties, and can be used for practical application in environmental issues.

Introduction

Semiconductor nanomaterials have shown their unique advantages in environmental science due to their excellent photocatalytic performance. Numerous reports are presented for dealing with various environmental remediation problems recently by semiconductor nanomaterials.[1–2] Photocatalysis is one of the most efficient ways for degradation of organic pollutants in water and air. Semiconductor oxides, such as α-Fe_2O_3, TiO_2, SnO_2 and ZnO, are found to be effective photocatalysts for the degradation of pollutants.[3–6] However, single component semiconductor possesses lot of disadvantages, such as low visible light utilization, high recombination rate of electron–hole pairs. Moreover, utilization of UV light as the source for photocatalysis is another major disadvantage of these photocatalysts. For instance, TiO_2 is a well-known semiconductor with wide bandgap, its photocatalytic property is restricted due to the usage of UV light as the source.[7]

In order to improve the utilization efficiency of visible light and reduce the recombination rate of electron–hole pairs, various kinds of composite nanoparticles are proposed, such as combination of narrow/wide bandgap semiconductors,[8–9] *p–n* heterojunction,[10] coupling of semiconductor and noble metals.[11] The noble metals (such as Au and Ag) are employed in photocatalytic system in recent years due to their localized surface plasmon resonance (LSPR) effect. A combination of semiconductor and noble metals composite system could be excited by visible light irradiation for the degradation of organic pollutants, which have attracted more interests in the field of photocatalysis.[12–13] After coupled with Au or Ag, the region of light harvesting has been extended into visible light. In addition, as a novel semiconductor, AgX (X = Cl, Br, I) can form a composite with metallic Ag as plasmon-induced photocatalyst. This new photocatalytic system has been developed rapidly because of its efficient visible light-driven photocatalytic properties.[14–15] Nevertheless, controlled fabrication of heterostructures with well-defined morphology is still a challenge in materials science. For instance, electron–hole pairs recombine easily due to irregular morphology before transferring to the photocatalyst surface in Ag/AgX particles, which results in the low efficiency of plasmonic photocatalytic system.[16]

Nanosized Ag/AgX hybrid particles are preferred to improve the photocatalytic performance with high separation efficiency of electron hole pairs via coupling with semiconductor. The combination of semiconductor and Ag/AgX hybrid nanoparticles has attracted more attention in enhanced photocatalytic application. The main reason is the fast electron/carrier transfer occurs

[a] *Key Laboratory of Artificial Micro– and Nano–structures of Ministry of Education, School of Physics and Technology, Wuhan University, Wuhan 430072, P. R. China. Tel: +86-27-68778529. Fax: +86-27-68778433. E-mail: weiwu@whu.edu.cn (W. Wu), xxh@whu.edu.cn (X.H. Xiao).*
[b] *Laboratory of Printable Functional Nanomaterials and Printed Electronics, School of Printing and Packaging, Wuhan University, Wuhan 430072, P. R. China.*
[c] *Department of Physics and Materials Science, City University of Hong Kong, Hong Kong SAR, P. R. China. E-mail: val.roy@cityu.edu.hk (V.A.L. Roy).*
†Electronic supplementary information (ESI) available: SEM images α-Fe_2O_3@Ag SNTs and α-Fe_2O_3@Ag/AgCl SNTs prepared under different react condition; UV-visible absorption spectra of α-Fe_2O_3, α-Fe_2O_3@Ag and α-Fe_2O_3@Ag/AgCl SNTs. See DOI: 10.1039/x0xx00000x

between metallic Ag with AgX or semiconductor nanoparticles. Moreover, most of the semiconductors in the hybrids system could also be excited in producing electron and hole for enhanced photocatalytic activity.[17–18] Iron oxide nanoparticles are the most significant nanomaterials in photocatalytic application. Especially, the α-Fe_2O_3 is one of the most common magnetic iron oxide materials that are chemically stable. It is also an n-type semiconductor with narrow band gap (2.2 eV), which is a visible light-driven photocatalyst.[19–20] Therefore, coupling of iron oxide nanoparticles with Ag/AgX to form the composite photocatalyst is a favorable way to improve the photocatalytic activity with an added value as magnetic recyclable photocatalyst. Moreover, the contact potential difference (CPD) at interface between the iron oxide@Ag/AgX is playing a vital role in charge transfer.

Recently, An and co-workers have synthesized a core–shell Fe_3O_4@SiO_2@AgCl:Ag nanocomposite for enhanced photocatalytic performance and the Fe_3O_4 represents as a recyclable catalyst carrier. Thus, only AgCl:Ag nanoparticles have made a contribution to the photocatalytic activity.[21] However, to the best of our knowledge, the controllable fabrication of the α-Fe_2O_3@Ag/AgCl hybrid photocatalytic system with well-defined shape remains scarce in literature. Herein, a novel tube-like α-Fe_2O_3@Ag/AgCl hybrid nanostructure has been fabricated as a photocatalyst operational under diverse light (simulated sunlight, UV light and visible light) illumination. The hybrid nanostructures are synthesized by three steps process. Firstly, α-Fe_2O_3 SNTs are synthesized by anion-assisted hydrothermal route. Then, Ag nanoparticles are anchored on the surface of α-Fe_2O_3 SNTs by silver mirror reaction and the final products have been obtained *via* oxidation of Ag with $FeCl_3$ solution. For the preparation of α-Fe_2O_3@Ag/AgCl, variation in Ag nanoparticles loading density under different $FeCl_3$ oxidant addition has also been investigated for optimizing photocatalytic activity. In comparison with the naked α-Fe_2O_3 and α-Fe_2O_3@Ag SNTs, the α-Fe_2O_3@Ag/AgCl SNTs samples exhibit superior photocatalytic activity, even better than commercially available P25 under simulated sunlight and UV light illumination. Our results demonstrate that control over experimental parameters could be the key factor for tailoring the photocatalytic performance of various heterostructure. Finally, we explain the corresponding photocatalytic mechanism behind the enhancement.

Experimental

Materials and Chemicals

$FeCl_3{\cdot}6H_2O$, Na_2SO_4, $NaH_2PO_4{\cdot}2H_2O$, $Na_2HPO_4{\cdot}12H_2O$, glutaraldehyde aqueous solution ($C_5H_8O_2$, 25%), silver nitrate ($AgNO_3$), Ammonia ($NH_3{\cdot}H_2O$, 25%) and ethanol (C_2H_5OH) were purchased from Sinopharm Chemical Reagent Co., Ltd., 3-aminopropyltrimethoxysilane (APTES) was purchased from Shanghai Jingchun Chemical Reagent Co., Ltd., Rhodamine B (RhB), Acid Orange 7 (AO7) and Malachite Green (MG) were purchased from Shanghai Aladdin Reagents Co., Ltd., polyvinylpyrrolidone (PVP, M.W. 10000 g/mol) was purchased from Sigma-Aldrich Co. The water used in the experiments was ultrapure water (18.2 Ω).

Synthesis of α-Fe_2O_3 SNTs

An anion-assisted hydrothermal route was carried out for the preparation of the monodisperse α-Fe_2O_3 SNTs.[22–23] Briefly, 0.27 g of $FeCl_3{\cdot}6H_2O$, 7 mg of NaH_2PO_4, and 19.5 mg of Na_2SO_4 were dissolved in 25 mL of H_2O under stirring, and then transferred to a 30 mL Teflon-lined stainless steel autoclave. This reaction was carried out at 220 °C for 12 h. Subsequently, the reactants were cooled down to room temperature naturally, the obtained α-Fe_2O_3 SNTs were washed several times with ethanol and deionized water. Finally, the product was obtained after drying under vacuum at 60 °C for 12 h.

Synthesis of α-Fe_2O_3@Ag SNTs

The α-Fe_2O_3/Ag composite SNTs were prepared by three steps. Firstly, 40 mg of α-Fe_2O_3 SNTs were dispersed in 100 mL of ethanol, 0.5 mL of APTES ethanol solution (2%, v/v) and 1 mL of water were then added. This reaction was kept under stirring at 30 °C for 3 h. The obtained products were centrifuged, washed with ethanol and water for three times, respectively. Then, aldehyde functionalized α-Fe_2O_3 SNTs were fabricated. The glutaraldehyde aqueous solution (10 mL, 25%) and phosphate buffer (PB) solution (2 mL. 0.02 M) were first dispersed in 35 ml water. The amino functionalized α-Fe_2O_3 SNTs were dispersed in above-mentioned solution with rapid stirring at 30 °C for 2 h. After that, centrifugation and washing process were carried out for obtaining the product. Finally, Ag NPs were anchored on the surface of α-Fe_2O_3 SNTs. The aldehyde-modified α-Fe_2O_3 was dispersed in 3 mL of ethanol; 5 mL deionized water of dissolving 34 mg $AgNO_3$ are prepared with diluted ammonia (4%) to form the silver-ammonia solution. Then, the two solutions were mixed and heated at 80 °C for 40 min. The final α-Fe_2O_3@Ag SNTs was dried under vacuum at 60 °C after centrifugation.

Synthesis of α-Fe_2O_3@Ag/AgCl SNTs

In a typical process, certain amount of as-synthesized α-Fe_2O_3/Ag composite SNTs was dispersed in an aqueous solution containing 50 mM PVP. Then, 3 mL of $FeCl_3$ (0.37 mol/L) was added drop wise into the solution. The resulting mixture was maintained at 30 °C for 30 min and vigorously stirred throughout the process. The products were washed with water and ethanol for three times. Finally, α-Fe_2O_3/Ag/AgCl Composite NPs were obtained.

Characterization

Scanning electron microscopy (SEM) images were performed by a cold field emission SEM (Hitachi S-4800). The transmission electron microscopy (TEM), high-resolution transmission electron microscopy (HRTEM), energy–dispersive X-ray spectroscopy (EDX) and selected area electron diffraction (SAED) analysis were carried out by JEOL JEM-2100F. X-ray photoelectron spectroscopy (XPS) analysis was performed by using Thermo Scientific ESCALAB 250 Xi system with Al Kα (1486.6 eV) as the radiation source. Powder X-ray diffraction (XRD) patterns were carried out by X'Pert Pro (Holland PANalytical) with Cu Kα radiation (λ = 0.1542 nm) operated at 40 kV, 40 mA and at a scan rate of 0.05° 2θ s^{-1}. The UV–Vis absorption spectra of the samples were performed by a Shimadzu UV-2550 spectrophotometer.

Photocatalytic Tests

The photocatalytic tests were carried out under three different kinds of light: simulated sunlight (mercury light), visible light and UV light irradiation. The control [10 mL RhB solution (10 $mg{\cdot}L^{-1}$) without added particles] and experimental [10 mL RhB solution (10 $mg{\cdot}L^{-1}$) with 3 mg of added particles] groups were tested for photocatalytic property. Firstly, the absorption of samples was present in the dark environment (30 min) for the absorption equilibrium. Then, the solutions were illuminated under three different lights such as simulated sunlight, visible light (λ > 420 nm) and UV light (λ < 420 nm) (the source is a mercury lamp (300 W) of BL–GHX–V photochemical reaction apparatus, and for the UV or visible light irradiation filters had been added). For every 5 min, the concentration of RhB was measured by UV–Vis spectra (measured in the range of 450 to 650 nm). The Shimadzu 2550 UV–Vis spectrophotometer was used to monitor the degradation progress of RhB dye.

Results and discussion

The morphology of α-Fe_2O_3@Ag/AgCl heterostructures

The synthesis process of tube-like α-Fe_2O_3@Ag/AgCl plasmonic photocatalyst includes three steps and the schematic illustration of the process is described in **Figure 1.** Firstly, the α-Fe_2O_3 SNTs are fabricated by hydrothermal route *via* utilization of anion ($H_2PO_4^-$ and SO_4^{2-}) as structure–guided agents. Then, the α-Fe_2O_3@Ag composite NPs are prepared via step-by-step technique, in which the α-Fe_2O_3 SNTs are firstly modified with an amino group (–NH_2) by APTES, and then to an aldehyde group (–CHO) *via* Schiff base reaction, and finally the Ag nanoparticles are deposited on the surface by a classic silver mirror reaction.[24] The Ag nanoparticles on the surface of α-Fe_2O_3 SNTs are partially transformed into AgCl nanoparticles *via* Fe^{3+} *in situ* oxidation in aqueous solution, and the plasmonic heterostructures are finally generated. In this hybrid nanostructure, the band gap of α-Fe_2O_3 and AgCl is 2.2 eV and 3.26 eV, respectively.[25-26] In this system, the narrow bandgap semiconductor of α-Fe_2O_3 with a wide bandgap semiconductor of AgCl combined with noble metal Ag is a way to reduce the recombination of electron and hole pairs[7].

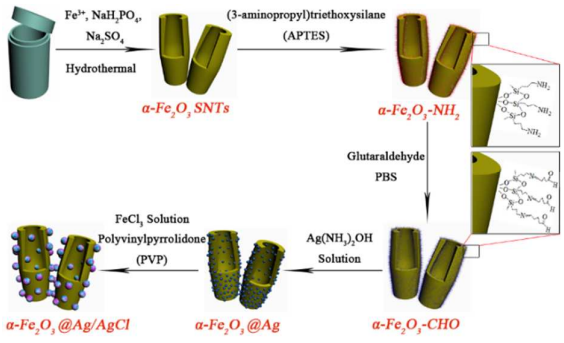

Figure 1. Schematic illustration of the formation process of α-Fe_2O_3@Ag/AgCl plasmonic heterostructures.

Figure 2 shows the morphology and composition of α-Fe_2O_3 SNTs. As shown in **Figure 2a**, the α-Fe_2O_3 SNTs present obviously open-at-both-ends with an average length and outer diameter of 547 and 237 nm, respectively. From the EDX analysis in **Figure 2b**, the Fe and O elements are identified. Moreover, the TEM image of α-Fe_2O_3 SNTs is presented in **Figure 2c**, the hollow structure could be further observed from the different electron-density. The average tube-wall thickness of α-Fe_2O_3 SNTs is about 20 nm. The HRTEM image is shown in **Figure 2d**, a clear lattice spacing of 0.221 and 0.270 nm could be indexed to (113) and (104) planes respectively, and it indicates a rhombohedral hematite structure (JCPDS No. 33–0664) of α-Fe_2O_3 SNTs. The inset SAED pattern in **Figure 2d** also shows a distinct polycrystalline structure owing to the diffraction rings. Above results indicate the successful synthesis of α-Fe_2O_3 SNTs.

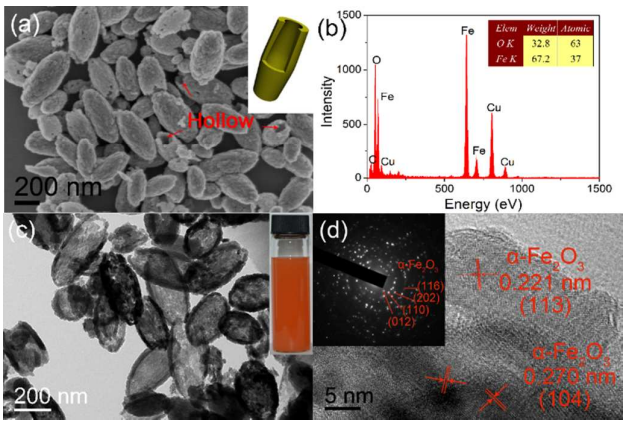

Figure 2. (a) SEM image of as-prepared α-Fe_2O_3 SNTs, the insert is the simulated 3D pattern of α-Fe_2O_3 SNTs, (b) EDX spectrum of α-Fe_2O_3 SNTs, (c) TEM image of α-Fe_2O_3 SNTs, the insert is the photograph of α-Fe_2O_3 SNTs which was dispersed in ethanol, (d) HRTEM image of as-prepared α-Fe_2O_3 SNTs (taken from the edge region), the insert is the corresponding SAED pattern.

Subsequently, the uniform α-Fe_2O_3@Ag composite SNTs have been synthesized by three steps. The morphologies and the as-obtained α-Fe_2O_3@Ag composite SNTs are presented in **Figure 3**. The SEM image of α-Fe_2O_3@Ag composite SNTs is displayed in **Figure 3a.** Obviously, numerous Ag NPs are anchored on the surface of α-Fe_2O_3 NPs. Furthermore, this feature is further confirmed by the TEM image (**Figure 3c**). Generally, Ag NPs are absorbed on the outer surface and inner surface of the α-Fe_2O_3 SNTs. The average size of Ag nanocrystals is about 22 nm. The Ag signals are also seen in EDX spectrum in **Figure 3b**. From the high-resolution TEM image, **Figure 3d**, the lattice spacing of 0.236 nm corresponds to the (111) plane of Ag nanoparticles (JCPDS No. 04–0783), and the lattice spacing of 0.221 nm belongs to the (113) plane of α-Fe_2O_3 SNTs. Additionally, the SAED pattern exhibit different diffraction rings that are assigned to α-Fe_2O_3 SNTs and metallic Ag, respectively (the insert of **Figure 3d**). These results show the formation of Ag loaded α-Fe_2O_3 SNTs. To obtain best photocatalytic activities of final products, the α-Fe_2O_3@Ag composite SNTs with the decoration of different Ag ions have been produced and verified. The SEM images of α-Fe_2O_3@Ag SNTs with different Ag ions (0.1, 0.2, 0.4 and 0.8 mM) loading are shown in **Table1** and **Figure S1** (*Supporting Information*). The distribution density of Ag nanoparticles on the surface of α-Fe_2O_3 SNTs increases with the addition of Ag ions.

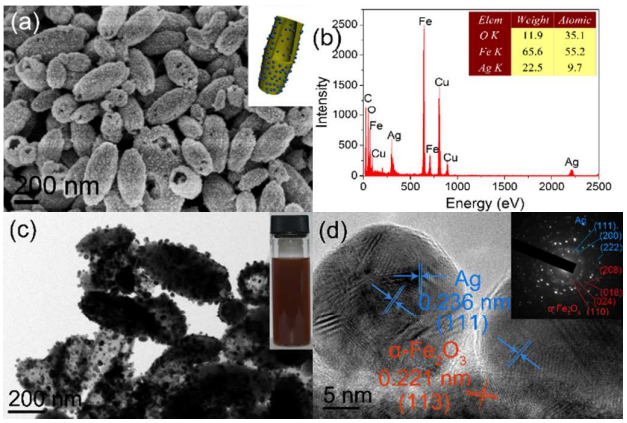

Figure 3. (a) SEM image of as-prepared α-Fe_2O_3@Ag SNTs, the insert is the simulated 3D pattern of α-Fe_2O_3@Ag SNTs, (b) EDX spectrum of α-Fe_2O_3@Ag SNTs, (c) TEM image of α-Fe_2O_3@Ag SNTs, the insert is the photograph of α-Fe_2O_3@Ag SNTs which was dispersed in ethanol, (d) HRTEM image of as-prepared α-Fe_2O_3@Ag SNTs (taken from the edge region), the insert is the corresponding SAED pattern.

Finally, the Ag nanoparticles on the surface of α-Fe_2O_3 SNTs were oxidized by $FeCl_3$ solution partially for the synthesis of α-Fe_2O_3@Ag/AgCl hybrid SNTs. The morphologies of α-Fe_2O_3@Ag/AgCl SNTs (sample 2, S2) are presented in **Figure 4**. The SEM image of α-Fe_2O_3@Ag/AgCl SNTs is depicted in **Figure 4a.** The Ag/AgCl hybrid nanoparticles on the surface grow larger than the Ag nanoparticles (**Figure 3a**), and the average diameter of Ag/AgCl hybrid nanoparticles is 40 nm. Indeed, the Ag nanoparticles could be partly oxidized into Ag ions to combine with Cl ions to form AgCl precipitation. The AgCl precipitation could aggregate with Ag nanoparticles to form larger size hybrid structure.[27] The main driving force is the reduction of the surface energy. Moreover, the element of Cl could be found in EDX spectrum with 2.7 % atomic ratio in **Figure 4b**, and the atomic ratio of element Ag is 10.6 %, these data indicate preliminarily that the metallic Ag are not transformed into AgCl nanoparticles completely. The hybrid structure of Ag/AgCl nanoparticles could be further confirmed by TEM and HRTEM images. The lattice spacing of 0.368 nm corresponds to the (012) plane of α-Fe_2O_3 SNTs, and lattice spacing of 0.236 nm belongs to (111) plane of metallic Ag. Furthermore, the lattice spacing of 0.203 and 0.248 nm correspond to (110) and (102) planes of AgCl (JCPDS No. 22−1326), respectively. The SAED pattern exhibits the respective diffraction rings of α-Fe_2O_3, Ag and AgCl. The above results demonstrate that α-Fe_2O_3@Ag/AgCl SNTs have been successfully fabricated by *in-suit* oxidation method.

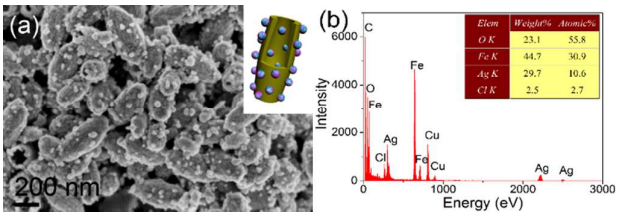

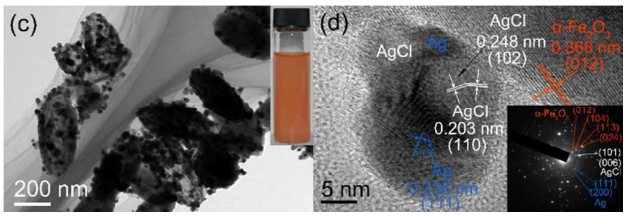

Figure 4. (a) SEM image of as-prepared α-Fe_2O_3@Ag/AgCl SNTs (S2), the insert is the simulated 3D pattern of α-Fe_2O_3@Ag/AgCl SNTs, (b) EDX spectrum of α-Fe_2O_3@Ag/AgCl SNTs, (c) TEM image of α-Fe_2O_3@Ag/AgCl SNTs, the insert is the photograph of α-Fe_2O_3@Ag/AgCl SNTs which was dispersed in ethanol, (d) HRTEM image of as-prepared α-Fe_2O_3@Ag/AgCl SNTs (taken from the edge region), the insert is the corresponding SAED pattern.

Moreover, in order to find the influence of $FeCl_3$ oxidant on its photocatalytic activities, different concentration of $FeCl_3$ oxidants have been added [0.5 (S1, **Figure S2a**), 1.0 (S2, **Figure S2b**), 1.5 (S3, **Figure S2c**), 2.0 mL (S4, **Figure S2d**); 0.37mol/L] for the synthesis of α-Fe_2O_3@Ag/AgCl as shown in **Table 1** and **Figure S2** (Supporting Information). The SEM images show that the Ag/AgCl nanoparticles are driven by low surface energy to escape from the α-Fe_2O_3 SNTs surface to form larger particles (**Figure S2c, S2d**). More Ag particles could be oxidized into Ag ions along with the increased $FeCl_3$. Most of the metallic Ag have been dislodged from the surface of α-Fe_2O_3 SNTs and re-deposited by AgCl precipitation. This precipitation could aggregate with some pure Ag nanoparticles to form large hybrid nanoparticles on the surface of α-Fe_2O_3 SNTs due to the reduced surface energy.

The samples of S5, S6, and S7 have been synthesized by the reaction of α-Fe_2O_3@Ag SNTs with different Ag loading amount (obtained from different Ag ions concentrations of 0.1, 0.2, 0.4 and 0.8 mM, **Figure S1**) and 1 mL of $FeCl_3$ solution (0.37 M). The experimental parameters and corresponding SEM images are depicted in **Table 1** and **Figure S3**, respectively. The images of **Figure S3a**, **S3b** and **S3d** are denoted as S5, S6 and S7, respectively. The image of **Figure S3c** is from S2 in **Figure S2b**. Similar to the α-Fe_2O_3@Ag/AgCl SNTs in the **Figure S2c, S2d**, the Ag/AgCl nanoparticles in **Figure S3a and S3b** are slipped out of α-Fe_2O_3 surface. On the other hand, an increase in Ag loading anchors more Ag/AgCl nanoparticles on the surface of α-Fe_2O_3 SNTs.

Table 1. Summary of the synthetic condition of samples and the kinetic rate constants (*k*) of photocatalytic RhB dye under mix light and visible light.

Sample	Molar quantity of $AgNO_3$ (mM) for synthesis of α-Fe_2O_3@Ag	Volume of $FeCl_3$ (mL) (0.37 M) For synthesis of α-Fe_2O_3@ Ag/AgCl	Ag : Fe^{3+}	*k* value for photocatalytic RhB dye (10^{-2} min^{-1})		
				Mix light	Visible light	UV light
Bare	/	/	/	0.393	0.059	0.283
α-Fe_2O_3	/	/	/	0.978	0.379	0.537
F@Ag	0.4	/	/	0.972	0.136	0.153
P25	/	/	/	4.22	2.76	7.21
S1	0.4	0.5	1 : 0.4625	15.0	0.894	12.3

S2	0.4	1	1 : 0.925	26.78	1.78	13.4
S3	0.4	1.5	1 : 1.3875	20.3	1.41	4.22
S4	0.4	2	1 : 1.85	11.2	0.617	5.68
S5	0.1	1	1 : 3.7	6.19	0.334	2.08
S6	0.2	1	1 : 1.85	6.09	0.525	0.933
S7	0.8	1	1 : 0.4625	11.7	1.34	7.15

The structural characterization of α-Fe_2O_3@Ag/AgCl heterostructures

The structural characterizations were carried out by powder X-ray diffraction (XRD) and X-ray photoelectron spectroscopy (XPS). **Figure 5** shows the XRD patterns of α-Fe_2O_3 SNTs (curve a) and α-Fe_2O_3@Ag SNTs (curve b) and α-Fe_2O_3@Ag/AgCl SNTs (curve c). The standard JCPDS card of pure α-Fe_2O_3 (33−0664, black lines), Ag (04−0783, blue lines) and AgCl (31−1238, magenta lines) are kept for comparison. The position and intensity of diffraction peaks of α-Fe_2O_3 SNTs in curve (a) could be indexed well with the standard JCPDS card (No. PDF# 33−0664). It indicates that as-prepared α-Fe_2O_3 SNTs are pure rhombohedral structure of hematite with high crystallinity. Moreover, the diffraction peaks of metallic Ag can be clearly identified from the curve (b) and can be indexed to the (111), (200), (220) and (311) planes of metallic Ag. The curve (c) is the XRD pattern of α-Fe_2O_3@Ag/AgCl SNTs (S2). Obviously, the diffraction peaks of AgCl nanoparticles are clearly found in curve (c) that could be indexed to (111), (200), (220), (311), (222) and (420) planes of chlorargyrite. It is noteworthy that the weak diffraction peaks of Ag could also be found in (111) plane due to the small grain of Ag and it is partly encapsulated by AgCl nanoparticles.[28−29]

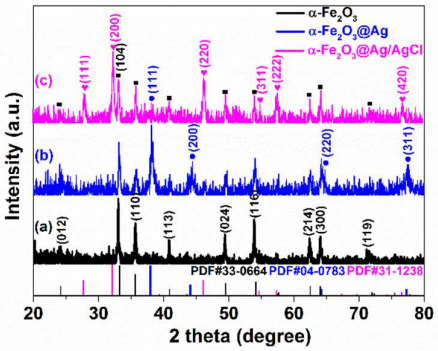

Figure 5. XRD patterns of as-prepared α-Fe_2O_3 SNTs (a), α-Fe_2O_3@Ag SNTs (b), α-Fe_2O_3@Ag/AgCl SNTs (S2, c), standard PDF cards of α-Fe_2O_3 (33−0664, black lines), metallic Ag (04−0783, blue lines) and pure AgCl (31−1238, fuchsin lines); The labels of ■, ● and ♥ are the corresponding peaks of α-Fe_2O_3, Ag, and AgCl, respectively.

Furthermore, the XPS spectrum of α-Fe_2O_3@Ag and α-Fe_2O_3@Ag/AgCl SNTs (S2) are also presented in **Figure 6**. **Figure 6a** shows the full XPS spectra of α-Fe_2O_3@Ag and α-Fe_2O_3@Ag/AgCl SNTs, respectively. The survey spectra of α-Fe_2O_3@Ag and α-Fe_2O_3@Ag/AgCl SNTs contain the peaks of Fe 2p and Ag 3d, and Ag $3p_{1/2}$, Ag $3p_{3/2}$. Nevertheless, the Ag 3d, Ag 3p peaks in α-Fe_2O_3@Ag/AgCl SNTs are weaker than in α-Fe_2O_3@Ag SNTs. The main reason is the formation of the large AgCl particles and the reduction of Ag element density on the surface of α-Fe_2O_3 SNTs. The new peaks of Cl 2p and Cl 2s emerge in α-Fe_2O_3@Ag/AgCl SNTs indicating the existence of AgCl in the hybrid nanostructure. **Figure 6b** displays the high resolution XPS spectrum of Fe 2p peaks. The two peaks located at 725.1 and 711.5 eV are attributed to Fe $2p_{1/2}$ and Fe $2p_{3/2}$ of α-Fe_2O_3, respectively. Their corresponding satellite peaks of 717.1 and 732.6 eV are attributed to characteristic absorption of Fe^{3+} in Fe_2O_3.[30] **Figure 6c** shows the XPS spectra of Ag 3d peak in α-Fe_2O_3@Ag and α-Fe_2O_3@Ag/AgCl (S2). The positions of Ag element in curve (b) are quite different from the curve (a). These two peaks can be divided into four peaks at the position of 374.0, 368.0 eV, 373.2, and 367.2 eV, the peaks at 374.0 and 368.0 eV can be attributed to metallic Ag, whereas the peaks at 373.2 and 367.2 eV can be attributed to AgCl. The binding energy position of metallic Ag could match well with the position in curve (a). This phenomenon indicates that both metallic Ag and Ag ions exist in the system. Moreover, **Figure 6d** shows the high resolution XPS spectrum of Cl 2p peak from α-Fe_2O_3@Ag/AgCl (S2). The overlapped peaks of Cl $2p_{1/2}$ and Cl $2p_{3/2}$ have been studied by peak−differentiating and imitating analysis. The divided peaks are located at 199.4 and 197.7 eV for Cl $2p_{1/2}$ and Cl $2p_{3/2}$, respectively. The XPS results further confirm that the formation of α-Fe_2O_3@Ag/AgCl SNTs.

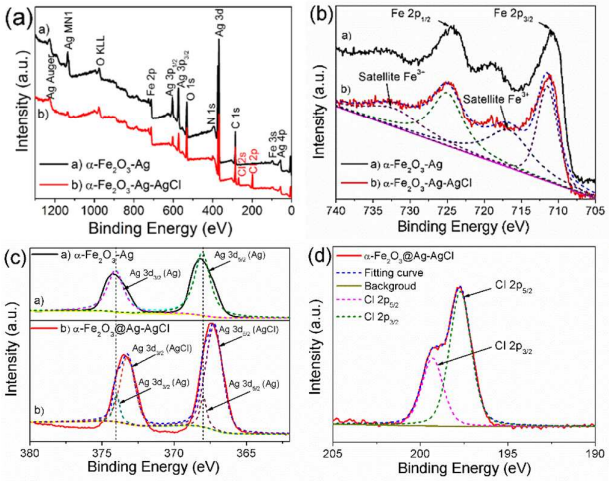

Figure 6. (a) The complete XPS spectra of α-Fe_2O_3@Ag (black line, a)) and α-Fe_2O_3@Ag/AgCl (red line, b), S2); (b) main and satellite peaks of Fe 2p3/2 and Fe 2p1/2 for the two samples; (c) main peaks of Ag 3d5/2 and Ag 3d3/2 peak for the α-Fe_2O_3/Ag and α-Fe_2O_3@Ag/AgCl (S2); (d) main peaks of Cl 2p3/2 and Cl 2p5/2 peaks for the α-Fe_2O_3@Ag/AgCl (S2).

The photocatalytic performance of α-Fe_2O_3@Ag/AgCl heterostructures

The UV−Vis absorption spectra of α-Fe_2O_3 SNTs (a), α-Fe_2O_3@Ag (b) and α-Fe_2O_3@Ag/AgCl SNTs (c) are presented in **Figure S4a.** The α-Fe_2O_3 SNTs show a visible absorption range from 380 to 600 nm for the narrow band gap α-Fe_2O_3 (~2.2 eV) (curve a).[31] After Ag deposition, the α-Fe_2O_3@Ag sample (curve b) presents a stronger and wider absorption in visible region than α-Fe_2O_3 SNTs by SPR absorption of metallic Ag. The red-shift could be ascribed to the introduction of Ag NPs. Moreover, the UV−Vis spectra of α-Fe_2O_3@Ag/AgCl SNTs (curve c) are shown. The absorption position

of α-Fe_2O_3@Ag/AgCl SNTs in UV region is improved due to the AgCl nanoparticles. However in the visible region the absorption intensity is reduced in comparison with α-Fe_2O_3@Ag SNTs. The transmittivity of the α-Fe_2O_3, α-Fe_2O_3@Ag and α-Fe_2O_3@Ag/AgCl are also tested, and the $(\alpha hv)^2$-hv curves of α-Fe_2O_3, α-Fe_2O_3@Ag and α-Fe_2O_3@Ag/AgCl are shown **Fig. S4b**. The calculated band-gap of α-Fe_2O_3, α-Fe_2O_3@Ag and α-Fe_2O_3@Ag/AgCl is 2.38, 2.57 and 2.04 eV, respectively. The band-gap of the composite shift to narrow band-gap direct which revealed that more visible light could be absorbed.

The photocatalytic properties of α-Fe_2O_3@Ag/AgCl SNTs have been investigated *via* the degradion of Rhodamine B (RhB) under different light irradiation, including simulated sunlight (UV + visible light), visible light (λ > 420 nm) and UV light (λ < 420 nm). Before the illumination, all the catalysts were kept for absorption equilibrium in dark for 30min. The typical UV−Vis absorption spectra of RhB are displayed in **Figure 7a** with the present of sample 2 under simulated sunlight irradiation, and the irradiation time interval is kept as 5 minutes. The absorption intensity is decreased with the increased irradiation time. This phenomenon indicates the photocatalytic degradation of RhB dyes with the presence of α-Fe_2O_3@Ag/AgCl SNTs. More than 98 % of RhB is degraded after 15 minute irradiation. The comparison of photocatalytic activity of as-obtained α-Fe_2O_3@Ag/AgCl SNTs samples, naked α-Fe_2O_3 seeds, α-Fe_2O_3@Ag and P25 are presented in **Figure 7b**. C_0 and C are the initial concentrations and experimentally determined concentrations of RhB, respectively. During the process of degradation, the pseudo first order reaction happens. The chemical reaction can be explained as $-\ln(C/C_0)=kt$, the k is the apparent rate constant of the degradation, also is the slope of the linear fit in **Figure 7c**.[32] The degradation rate is proportional to the slope. As shown in **Table 1**, the k value for the pure α-Fe_2O_3 SNTs, α-Fe_2O_3@Ag and P25 are 0.978×10^{-2}, 0.972×10^{-2} and 4.22×10^{-2} min^{-1}, respectively. The lower photocatalytic activity of α-Fe_2O_3@Ag than pure α-Fe_2O_3 SNTs is due to the dark color of α-Fe_2O_3@Ag which prevents the light penetration.[33] But the k values of sample 1–7 are larger than that of all above mentioned values attributed to the enhanced plasmonic photocatalytic activity of α-Fe_2O_3@Ag/AgCl SNTs. The k value of sample 2 is the largest (26.78×10^{-2} min^{-1}) under simulated sunlight irradiation showing a significant advantage in photocatalytic degradation of RhB than other similar nanocomposites[34] or other iron oxide-noble metal-semiconductor system.[7] Moreover, the stability of α-Fe_2O_3@Ag/AgCl SNTs (S2) has been further investigated. The recycling process for RhB degradation is presented under simulated sunlight (**Figure 7d**). The stability of S2 is presented for 4 recycling times indicating an excellent photocatalytic stability of the system.

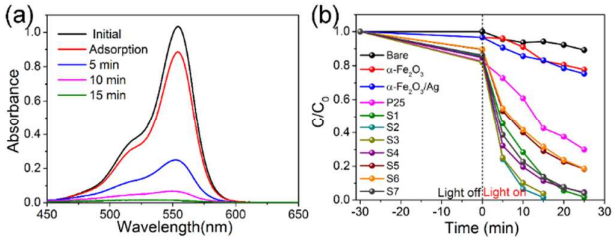

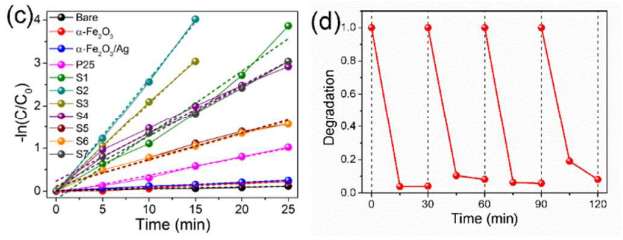

Figure 7. (a) The typical degradation curve of RhB in the presence of α-Fe_2O_3@Ag/AgCl SNTs (S2); (b) the normalized concentration changing of as-prepared samples under simulated sunlight irradiation; (c) the reaction rate constant versus irradiation time of simulated sunlight with different catalysts; (d) the recycled photodegrading the RhB under simulated sunlight irradiation for 30 min over the S2.

The photocatalytic properties of these samples were further investigated under visible light (λ > 420 nm) and UV light (λ < 420 nm) irradiation. **Figure 8a** show the comparison of photocatalytic activity of sample 1–7, naked α-Fe_2O_3 seeds, α-Fe_2O_3@Ag and P25 under visible light irradiation. The k values of these samples are displayed in **Figure 8b** and **Table 1**. From the data and figures, most of the samples are better than that of naked α-Fe_2O_3 seeds and α-Fe_2O_3@Ag. The Sample 2 (S2) shows the best photocatalytic performance among all samples, more than 90% RhB degrades within 120 min under visible light irradiation. **Figure 8c** show the comparison of photocatalytic activity of these samples under UV light irradiation. The S2 reveals the best photocatalytic activity (k =13.39×10^{-2} min^{-1}) than other samples such as naked α-Fe_2O_3 seeds and α-Fe_2O_3@Ag and P25 (**Figure 8d**).

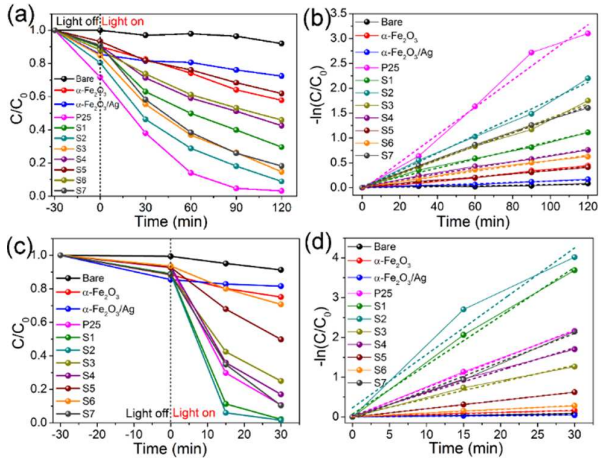

Figure 8. (a) (c) The normalized concentration changing of as-prepared samples under visible light (a) and UV light (c) irradiation; (b) (d) The corresponding reaction rate constant versus irradiation time of visible light (b) UV light (d) with different catalysts.

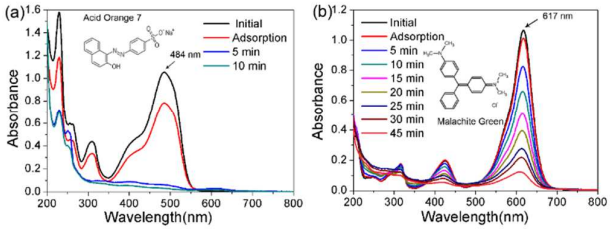

Figure 9. (a) The degradation curve of AO7 in the presence of α-Fe_2O_3@Ag/AgCl SNTs (S2); (b) The degradation curve of MG in the presence of α-Fe_2O_3@Ag/AgCl SNTs (S2).

Furthermore, the degradation process of another two dyes (Acid Orange 7 (AO7) and Malachite Green (MG)) are also studied under the simulated sunlight by using 3 mg Sample 2, respectively. **Fig. 9a** shows the UV-Vis absorption spectra of 10 mL of AO7 (15 mg/L). About 97% AO7 are degraded after 10 min irradiation of simulated sunlight. The UV-vis absorption spectra of 10 mL of MG (10 mg/L) are shown in **Fig. 9b**. After irradiation for 45 min, about 90% MG are degraded. Thus, this α-Fe_2O_3@Ag/AgCl heterostructures could degrade various organic pollutants.

The S2 presents the enhanced photodegradation rate under all three kinds of light irradiation. That indicates the excellent performance of α-Fe_2O_3@Ag/AgCl SNTs for the degradation of RhB under the optimized synthesis parameters [Ag : Fe^{3+} is about 1 : 0.925, 92.5% of the Ag are transferred to Ag^+, which are coincided with literature report.[27]]. Furthermore, under UV light irradiation, AgCl presents a strong photocatalytic activity than α-Fe_2O_3 and Ag. However, it is well known that AgCl could be reduced into metallic Ag under UV light irradiation, thus improving the photocatalytic activity under simulated sunlight irradiation.[35–36] Under simulated sunlight irradiation, the AgCl first absorbs the UV light for UV light photocatalysis and then partly transfer to metallic Ag for efficient plasmonic photocatalysis under visible light irradiation. However, under pure visible light irradiation, Ag and α-Fe_2O_3 SNTs can only be activated for the degradation of RhB. The irradiation energy is quite low after the elimination of UV light, thus the photocatalytic activity is poor. However, under UV light irradiation, AgCl present a strong UV light driven photocatalytic activity because of the strong oxidizability of Cl^0 free radical.[37]

Proposed mechanism

In this composite photocatalyst, the enhanced plasmonic photocatalytic activity of α-Fe_2O_3@Ag/AgCl SNTs is shown. The main reason behind the enhancement is the efficient interfacial charge rectification and faster carrier migration. **Figure 10** exhibits the enhanced catalytic mechanism under simulated sunlight, visible light and UV light. The band gaps of α-Fe_2O_3 and AgCl are 2.2 eV and 3.26 eV on the normal hydrogen electrode (NHE) scale, respectively.[26, 38] The work function of Ag is 4.8 eV,[39] and its position could be calculated at 0.3 eV on the NHE scale.

Under simulated sunlight irradiation, in S1, S2 and S7, as shown in **Figure 10a**, the metal Ag is activated by the near field enhancement of SPR effect to produce electrons in SPR states under visible light irradiation,[40–41] followed by the flow of photo-excited electrons to the conduction band (CB) of α-Fe_2O_3 SNTs. Moreover, the metal NPs can produce a strong localized surface electric field. The localized SPR of Ag NPs excites the surrounding semiconductor to produce more photogenerated electrons and holes.[42] Electrons are trapped by oxygen and H_2O in the solution, and the hydroxyl radical (·OH) are obtained through reaction.[7, 43] Other part of electrons are transferred to AgCl when they contact to each other. The hole in α-Fe_2O_3 SNTs are captured by H_2O to form hydroxyl radicals (·OH).

Furthermore, part of hole from metal Ag transfers to the surface of AgCl for oxidizing chloride ion to Cl^0 free radical.[44] However, the AgCl could also absorb the UV light because of the wide band-gap (3.26 eV), the Ag−Cl bonds breaks after the AgCl absorption of photons, and the electrons released from the chloride ion is excited from valence band (VB) to CB. The hole left on VB could oxidize chloride ion into Cl^0 free radical for highly reactive degradation of RhB, other part of hole could transfer to α-Fe_2O_3 SNTs. On the other hand, the as-produced electrons are trapped by Ag^+ which originates from AgCl to form the metallic Ag.[35–36] During this process, the visible light photocatalytic activity has been further improved. The photo-chemical process are demonstrated in these chemical equations:[40, 45]

$$\alpha\text{-}Fe_2O_3 + h\nu \rightarrow h^+ + e^- \quad (1)$$

$$Ag + h\nu \rightarrow h^+ + e^- \quad (2)$$

$$AgCl + h\nu \rightarrow Ag^+ + Cl^0 + e^- \quad (3)$$

$$Ag^+ + e^- \rightarrow Ag \quad (4)$$

$$h^+ + H_2O \rightarrow OH^\bullet + H^+ \quad (5)$$

$$2e^- + O_2 + 2H_2O \rightarrow 4\ OH^\bullet \quad (6)$$

$$h^+ + Cl^- \rightarrow Cl^0 \quad (7)$$

$$OH^\bullet + RhB \rightarrow CO_2 + H_2O \quad (8)$$

$$Cl^0 + RhB \rightarrow Cl^- + CO_2 + H_2O \quad (9)$$

However, Ag^0 is not been found in sample S3-S6. The Fermi level of α-Fe_2O_3 and AgCl nanoparticles will reach equilibrium when they contact with each other. The charge separation process are also exist between them. Compare with α-Fe_2O_3@Ag SNTs, the introducing of AgCl will enhance the photocatalytic abilities.

By comparing the photocatalytic activity of these samples, the reason of the best photocatalytic activity of S2 are explained as follows. The near field enhanced SPR effect of metal Ag in S1, S2 and S7 play an important roles for the enhanced photocatalytic performance. The Ag : AgCl in S2 is 7.5 : 92.5, this proportion in S2 show the best degradation efficiency among all samples. The metal Ag (7.5 %) show the SPR effect under visible light, but 92.5% of AgCl show a strong UV light-driven photocatalytic activity than SPR effect of metal Ag. Thus the photocatalytic activity of S2 is higher than S1 and S7 (53.75% of metal Ag and 46.25% of AgCl). Because of the SPR effect of metal Ag in S2, the photocatalytic activity of S2 is higher than S3, S4, S5 and S6. Therefore, the enhanced photocatalytic performance of S2 can be attributed to the synergetic effect of efficient UV light-driven photocatalytic activity and near field enhanced SPR effect.

Under visible light irradiation, in S1, S2 and S7, the low response of AgCl to the visible light is due to its wide band gap (3.26 eV). Only Ag and α-Fe_2O_3 SNTs contribute to the photocatalytic activity under visible light, but AgCl still plays an important role in visible light-driven photocatalysis. More AgCl provide more Cl^0 for degradation the organic pollutants. In these three samples, S2 possess more AgCl show the best photocatalytic activity. The specific charge transfer process are shown in **Figure 10b**, the near field SPR effect of Ag nanoparticles results in generating the electron−hole pairs. Firstly, the negatively charged surface (Cl^- ion terminal) of AgCl facilitates to polarize the free electrons in metallic Ag.[46-47] Thus, the

plasmon-excited holes transfer to the surface of AgCl nanoparticle, and the chloride ions oxidize into Cl^0 free radical by the holes. The Cl^0 show a strong catalytic activity for the degradation of RhB, after the degradation process, the Cl^0 is reduced into chloride ions. Subsequently, the Cl ions combine with Ag ions to maintain stability.[40, 45] Moreover, the plasmon-excited electrons in metallic Ag are transferred to the surface of α-Fe_2O_3 SNTs which are trapped by oxygen and H_2O for the degradation of RhB. However, in S3, S4, S5 and S6, only the α-Fe_2O_3 could absorb visible light, the part of electrons from α-Fe_2O_3 are transferred to AgCl nanoparticles for the charge separation. This reason could explain why the photocatalytic activity of these samples are higher than naked α-Fe_2O_3 SNTs. The photocatalytic efficiency of all the samples is inferior under simulated sunlight irradiation. The main reason is that the AgCl is the dominant ingredient in Ag/AgCl nanoparticles, and it cannot be reduced into metallic Ag without UV light irradiation.

Under UV light irradiation, AgCl play a dominant role in degradation of RhB (**Figure 10c**). In S1, S2 and S7, the electrons are excited from VB of AgCl, and transfer to CB, and then transfer to Ag. The part of holes generated in VB play a dominant role in photodegradation of RhB via the oxidation of Cl^- ion into Cl^0, other part of hole are transferred to α-Fe_2O_3 SNTs for effective charge separation. The effective charge separation could be attributed to two reasons. Firstly, the electrons in the conduction band are easily trapped by Ag ion to form metallic Ag. Furthermore, the redundant electrons could be transferred through the metallic Ag, and captured by O_2 in solution.[40, 48] In S3, S4, S5 and S6, the electrons cannot be transferred, only the hole could be transferred to α-Fe_2O_3 SNTs. Thus S2 with 92.5% AgCl and 7.5% metal Ag show the best photocatalytic activity under the UV light irradiation.

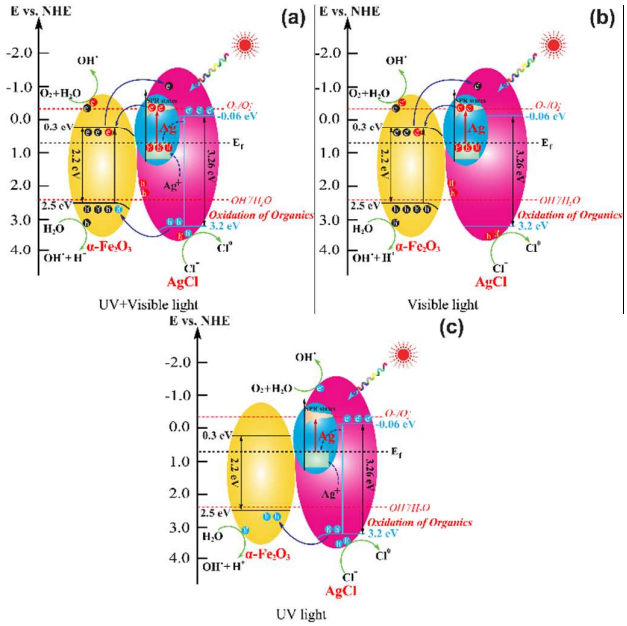

Figure 10. Schematic diagram of the photocatalytic mechanism and the way of electron–hole separation in α-Fe_2O_3@Ag/AgCl hybrid SNTs under simulated sunlight (a), visible light (b) and UV light (c) irradiation.

Conclusions

In conclusion, a tube-like α-Fe_2O_3@Ag/AgCl heterostructures have been synthesized by three steps process in a controlled manner. The α-Fe_2O_3 SNTs based composite nanomaterials with Ag/AgCl on the surface of hybrid nanoparticles facilitates the charge transfer among α-Fe_2O_3, Ag and AgCl during the plasmanic photocatalytic performance for the degradation of RhB under simulated sunlight, visible light and UV light, respectively. These α-Fe_2O_3@Ag/AgCl SNTs exhibit excellent photocatalytic activity than those bare α-Fe_2O_3 SNTs and α-Fe_2O_3@Ag and found to be even better than commercially available P25 under simulated sunlight and UV light irradiation. This strategy reveals that the plasmonic photocatalysts coupled with semiconductors can be a new design for efficient photocatalysis. Thus these tube-like α-Fe_2O_3@Ag/AgCl SNTs are expected to provide new perspectives for the fabrication of other plasmonic photocatalysts for enhanced plasmonic photocatalytic performance.

Acknowledgements

This work was supported by the NSFC (51201115, 51171132, 11375134), China Postdoctoral Science Foundation (2014M550406), Hong Kong Scholars Program, Hubei Provincial Natural Science Foundation (2014CFB261), the Fundamental Research Funds for the Central Universities and Wuhan University.

Notes and references

1 A. Mills, R. H. Davies and D. Worsley, *Chem. Soc. Rev.*, 1993, **22**, 417-425.
2 M. R. Hoffmann, S. T. Martin, W. Choi and D. W. Bahnemann, *Chem. Rev.*, 1995, **95**, 69-96.
3 W. Wu, S. Zhang, J. Zhou, X. Xiao, F. Ren and C. Jiang, *Chem. Eur. J.*, 2011, **17**, 9708-9719.
4 W. Wu, S. Zhang, F. Ren, X. Xiao, J. Zhou and C. Jiang, *Nanoscale*, 2011, **3**, 4676-4684.
5 W. Wu, S. Zhang, X. Xiao, J. Zhou, F. Ren, L. Sun and C. Jiang, *ACS Appl. Mater. Interfaces*, 2012, **4**, 3602-3609.
6 W. Wu, X. Xiao, S. Zhang, F. Ren and C. Jiang, *Nanoscale Res. Lett.*, 2011, **6**, 533.
7 L. Sun, W. Wu, S. Yang, J. Zhou, M. Hong, X. Xiao, F. Ren and C. Jiang, *ACS Appl. Mater. Interfaces*, 2014, **6**, 1113-1124.
8 J. SongáChen, S. ZhangáQiao and X. WenáLou, *Chem. Commun.*, 2011, **47**, 2631-2633.
9 W. Wu, C. Jiang and V. A. Roy, *Nanoscale*, 2015, **7**, 38-58.
10 Q. Tian, W. Wu, L. Sun, S. Yang, M. Lei, J. Zhou, Y. Liu, X. Xiao, F. Ren and C. Jiang, *ACS Appl. Mater. Interfaces*, 2014, **6**, 13088-13097.
11 W. Wu, L. Liao, S. Zhang, J. Zhou, X. Xiao, F. Ren, L. Sun, Z. Dai and C. Jiang, *Nanoscale*, 2013, **5**, 5628-5636.
12 K. Awazu, M. Fujimaki, C. Rockstuhl, J. Tominaga, H. Murakami, Y. Ohki, N. Yoshida and T. Watanabe, *J. Am. Chem. Soc.*, 2008, **130**, 1676-1680.
13 H. You, R. Liu, C. Liang, S. Yang, F. Wang, X. Lu and B. Ding, *J. Mater. Chem. A*, 2013, **1**, 4097-4104.
14 M. Zhu, P. Chen and M. Liu, *ACS Nano*, 2011, **5**, 4529-4536.
15 L. Ye, J. Liu, C. Gong, L. Tian, T. Peng and L. Zan, *ACS Catal.*, 2012, **2**, 1677-1683.
16 H. Zhang, X. Fan, X. Quan, S. Chen and H. Yu, *Environ. Sci. Technol.*, 2011, **45**, 5731-5736.

17 J. Hou, Z. Wang, C. Yang, W. Zhou, S. Jiao and H. Zhu, *J. Phy. Chem. C*, 2013, **117**, 5132-5141.
18 G. Begum, J. Manna and R. K. Rana, *Chem.-Eur. J.*, 2012, **18**, 6847-6853.
19 G. Liu, Q. Deng, H. Wang, D. H. Ng, M. Kong, W. Cai and G. Wang, *J. Mater. Chem.*, 2012, **22**, 9704-9713.
20 J. Zhu, Z. Yin, D. Yang, T. Sun, H. Yu, H. E. Hoster, H. H. Hng, H. Zhang and Q. Yan, *Energ. Environ. Sci.*, 2013, **6**, 987-993.
21 C. An, X. Ming, J. Wang and S. Wang, *J. Mater. Chem.*, 2012, **22**, 5171-5176.
22 W. Wu, X. Xiao, S. Zhang, J. Zhou, L. Fan, F. Ren and C. Jiang, *J. Phy. Chem. C*, 2010, **114**, 16092-16103.
23 W. Wu, X. Xiao, S. Zhang, T. Peng, J. Zhou, F. Ren and C. Jiang, *Nanoscale Res. Lett.*, 2010, **5**, 1474-1479.
24 S. Zhang, F. Ren, W. Wu, J. Zhou, L. Sun, X. Xiao and C. Jiang, *J. Nanopart. Res.*, 2012, **14**, 1-13.
25 S. Zhang, F. Ren, W. Wu, J. Zhou, X. Xiao, L. Sun, Y. Liu and C. Jiang, *PCCP*, 2013, **15**, 8228-8236.
26 Y. Li and Y. Ding, *J. Phys. Chem. C*, 2010, **114**, 3175-3179.
27 Y. Bi and J. Ye, *Chem. Commun.* , 2009, 6551-6553.
28 H. Remita, A. Etcheberry and J. Belloni, *J. Phy. Chem. B*, 2003, **107**, 31-36.
29 T. Yonezawa and N. Toshima, *J. Chem. Soc., Faraday Trans.*, 1995, **91**, 4111-4119.
30 J. F. Moulder, W. F. Stickle, P. E. Sobol and K. D. Bomben, *Handbook of X-ray photoelectron spectroscopy*, Perkin Elmer Eden Prairie, MN, 1992.
31 W. Wu, Z. H. Wu, T. Yu, C. Z. Jiang and W. S. Kim, *Sci. Technol. Adv. Mater.*, 2015, **16**, 023501.
32 J. Zhang, G. Chen, D. Guay, M. Chaker and D. Ma, *Nanoscale*, 2014, **6**, 2125-2130.
33 J. Lea and A. A. Adesina, *J. Photoch. Photobiol. A*, 1998, **118**, 111-122.
34 Y. Zhang, Y. Zhang and J. Tan, *J. Alloy. Compd.*, 2013, **574**, 383-390.
35 M. Lanz, D. Schürch and G. Calzaferri, *J. Photoch. Photobio. A*, 1999, **120**, 105-117.
36 K. Pfanner, N. Gfeller and G. Calzaferri, *J. Photoch. Photobio. A*, 1996, **95**, 175-180.
37 H. Wang, W. Cui, B. Han and Y. Liang, *Chem. Ind. Eng. Prog*, 2013, **32**, 346-351.
38 S. Linic, P. Christopher and D. B. Ingram, *Nat. Mater.*, 2011, **10**, 911-921.
39 J. Zhou, F. Ren, S. Zhang, W. Wu, X. Xiao, Y. Liu and C. Jiang, *J. Mater. Chem. A*, 2013, **1**, 13128-13138.
40 P. Wang, B. Huang, X. Qin, X. Zhang, Y. Dai, J. Wei and M. H. Whangbo, *Angew. Chem. Int. Edit.*, 2008, **47**, 7931-7933.
41 Y. Min, G. He, Q. Xu and Y. Chen, *J. Mater. Chem. A*, 2014, **2**, 1294-1301.
42 J. Long, H. Chang, Q. Gu, J. Xu, L. Fan, S. Wang, Y. Zhou, W. Wei, L. Huang and X. Wang, *Energ. Environ. Sci.*, 2014, **7**, 973-977.
43 S. S. Soni, M. J. Henderson, J. F. Bardeau and A. Gibaud, *Adv. Mater.*, 2008, **20**, 1493-1498.
44 J. Zhou, Y. Cheng and J. Yu, *J. Photoch. Photobio. A.,* 2011, **223**, 82-87.
45 Z. Mingshan, C. Penglei and L. Minghua, *Prog. Chem.*, 2013, **25**, 209-220.
46 B. Tian, R. Dong, J. Zhang, S. Bao, F. Yang, J. Zhang, *Appl. Catal. B Environ.,* 2014, **158**, 76-84.
47 C. An, S. Peng and Y. Sun, *Adv. Mater.*, 2010, **22**, 2570-2574.
48 P. Wang, B. Huang, X. Zhang, X. Qin, H. Jin, Y. Dai, Z. Wang, J. Wei, J. Zhan and S. Wang, *Chem.-Eur. J.*, 2009, **15**, 1821-1824.

Tube-like α-Fe_2O_3@Ag/AgCl Heterostructure: Controllable Synthesis and Enhanced Plasmonic Photocatalytic Activity

J. Liu, W. Wu, Q. Tian, S. L. Yang, L. L. Sun, X. H. Xiao*, F. Ren, C. Z. Jiang, V. A. L. Roy**

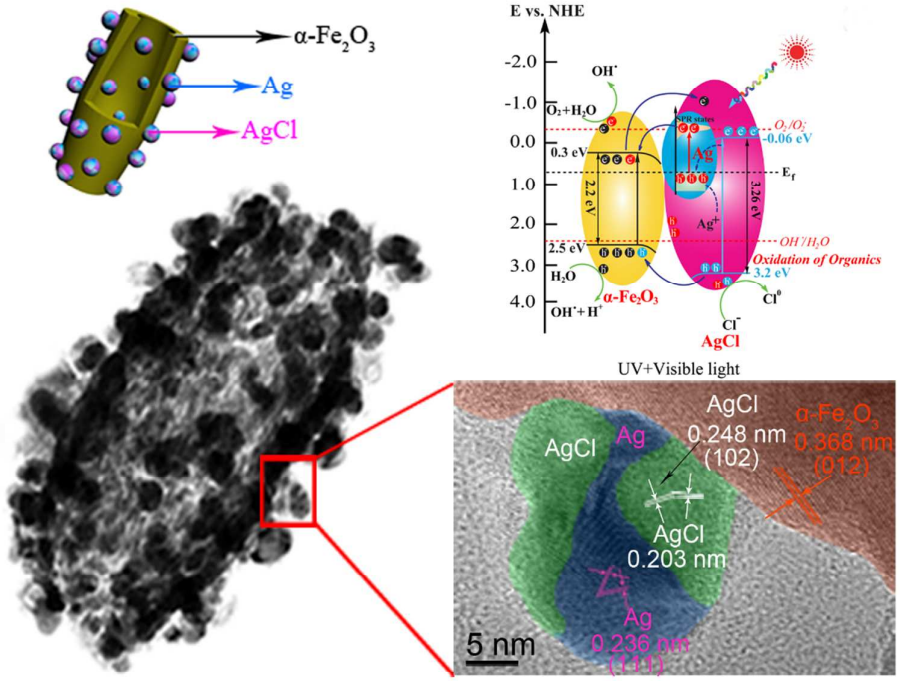

α-Fe_2O_3@Ag/AgCl heterostructures